

Imaging Spatially Extended Objects with Interferometers: Mosaicking and the Short Spacing Correction

Brian S. Mason¹

¹*National Radio Astronomy Observatory, Charlottesville, VA, USA;
bmason@nrao.edu*

Abstract. Interferometry is a powerful technique for making sensitive, high-fidelity images of the sky, but is limited in its ability to measure extended or diffuse emission. Better images of extended astronomical objects can be obtained by mosaicking together many pointings of the interferometer array. Even better images can be obtained by combining these data with data from a single-dish telescope. This lecture explains commonly practiced techniques for obtaining and analyzing these observations, and the theory behind them.

1. Introduction

An interferometer can make remarkably accurate measurements of the sky intensity, but the features that these measurements capture is limited by the length and orientation of the interferometer's baselines. The absence of information at spatial frequencies higher than that provided by the interferometer's *longest* baselines results in limited angular resolution, making features much smaller than the scale of $\theta_{min} = \lambda/b_{max}$ impossible to distinguish. The absence of information on angular scales larger than those measured by the interferometer's *shortest* baselines, $\theta > \theta_{max} \sim (\lambda/b_{min})$, can in many instances be even more problematic. The interferometer can sometimes be reconfigured to measure larger scales by having more, shorter baselines. However, since the baselines cannot be shorter than the dish diameter D , θ_{max} can never be larger than (λ/D) . The missing large-scale information corresponds to *missing flux* for spatially resolved objects; and can give rise, in effect, to variable local backgrounds that make it challenging to measure integrated flux densities, even of relatively compact objects. Since much astrophysics is done by comparing spatially integrated features at different wavelengths—*e.g.*, the integrated line intensity in two transitions, or the integrated continuum flux density at two widely separated frequencies—this can be a significant limitation.

This lecture will address two of the main methods to overcome this limitation: acquiring and jointly analyzing data from adjacent interferometer pointings, a technique known as *mosaicking*; and combining data from a single-dish telescope(s) with the interferometer data. In § 2, I will articulate the problem and present the mathematical and conceptual foundation for both of these methods, the Ekers-Rots theorem. We will see that the Ekers-Rots theorem implies that the shortest baseline b_{min} in fact contains information about scales $\theta > (\lambda/b_{min})$, and gives a conceptual scheme to retrieve that information from mosaicked interferometer observations. Several common approaches for analyzing interferometric mosaics are discussed in § 3. Techniques for combining

single dish and interferometer data are discussed in § 4, and some common “real-world” considerations are discussed in § 5.

A few general comments are in order. The purpose of this lecture is to explain the current, generally accepted best practices involved in interferometric imaging of spatially extended astronomical objects, and the theory behind these practices. The reader is presumed to be familiar with the basic concepts of synthesis imaging, such as the CLEAN algorithm for deconvolution. These foundational topics are covered in Taylor et al. (1999), and with greater depth and mathematical rigor in Thompson et al. (2017). The reader may also find the online lectures from recent Synthesis Imaging Workshops to be of use (e.g. Mioduszewski 2014; Marvil 2018). The field of astronomical imaging is dynamic, and consequently there are numerous new and exciting techniques under development that are applicable to the problems we consider. While pointers into this literature are provided, there is no attempt to survey these approaches systematically, which could constitute an article unto itself. In this article the clean deconvolution *algorithm* will be denoted as CLEAN; implementations of CLEAN (or other imaging algorithms) in particular packages will be indicated in typewriter font—`clean`, `tclean`, or `MOSMEM` for instance. Most of the practical examples in this lecture use the CASA package. At the time these lecture notes were posted the most recent CASA release was 5.6. In this and recent releases, the generally recommended implementation of CLEAN is the task called `tclean`.

2. Mosaicking Fundamentals

2.1. The Problem

There are two, related criteria by which a source can be considered “large” from the point of view of synthesis imaging:

1. The source is large compared to the scale measured by the shortest baseline b_{min} :
 $\theta_{src} > \lambda/b_{min}$.
2. The source is large compared to the antenna primary beam: $\theta_{src} > \theta_B$.

Here θ_B is the Full-Width at Half Maximum (FWHM) of the antenna primary beam; λ is the wavelength of the observation; and θ_{src} is the source size. As mentioned previously these two cases are related since θ_B is determined by the antenna diameter D ($\theta_B \approx \lambda/D$), and the shortest *possible* physically realizable value of b_{min} is also constrained by the dish diameter ($b_{min} > D$). Interferometric mosaicking can help in both cases, although in the second case supplementary single-dish data will often be required depending on the science goal and source morphology.

A related situation is that where the sources are compact by the above criteria but distributed over a region comparable to or larger than the antenna primary beam. Many interferometric surveys fall into this category, such as the NRAO VLA Sky Survey (NVSS: Condon et al. 1998) and the more recent VLA Sky Survey (VLASS: Lacy et al. 2020). These wide-field imaging cases require techniques — for instance, accurate modelling of the primary beam and accounting for the W-term— that can also apply to the cases we are considering here. For clarity our discussion will focus specifically on issues involved in imaging and flux recovery for objects that are large in the sense indicated. Note that for geometrical reasons, the W-term tends not to be significant for the types of compact configurations which are best for imaging extended sources.

We can refine the criterion by which a source is deemed to be “large” and gain some intuition by considering a simple example: measuring the visibility function on a single baseline of length b , for a sky brightness component which has a Gaussian shape with FWHM $= \theta_{src}$. As a proxy for the quality of information on a given angular scale, we consider the *ratio* of the measured visibility to the total flux density of the Gaussian component S_{src} , which can be shown to be:

$$\frac{V(b)}{S_{src}} = \frac{1}{1 + (\theta_{src}/\theta_B)^2} \text{Exp} \left(-4.71 \frac{(b/D)^2}{1 + (\theta_B/\theta_{src})^2} \right) \quad (1)$$

Here we have assumed the antenna primary beam FWHM $\theta_B = 1.15 \times (D/\lambda)$. This ratio is shown as a function of source size for three representative baseline lengths in Figure 1. Several facts are apparent. First, for a source as large as the primary beam ($\theta_B = \theta_{src}$), even the shortest physically realizable baseline ($b = D$) performs very poorly, recovering only 5% of the total flux density. For this reason, a typically quoted “largest angular scale” (LAS) that an interferometer can effectively measure¹ is $\theta_{LAS} = \frac{1}{2}(\lambda/b_{min})$. If the uv -coverage is poor, even this is an overestimate. Our single-baseline example measurement would detect $\sim 40\%$ of the total flux density of a Gaussian component of this size. Second, it is apparent that the decline in visibility with baseline length is very rapid. For instance, a $b = 2D$ baseline— which practically speaking is still a very short baseline— will recover only 4% of the total flux density for a Gaussian component with $\theta_{src} = \theta_{LAS} = \frac{1}{2}(\lambda/b_{min})$. Finally, the *increase* in the signal amplitude as the baseline gets shorter is (reciprocally) rapid: a hypothetical $b = D/2$ baseline contains much higher quality information about the large angular scales. The question is, can we make use of information from such ostensibly unphysical baselines? In the next section we will see that an interferometer can in fact recover much of the “missing”, often critically important short-spacing information, even without single-dish data.

A qualitative idea of the effect of missing short-spacings can be obtained by considering Figure 2. Imagining the interferometer uv -coverage as a uniform plateau— which has a Fourier transform of a Sinc() function— the short-spacing deficit can be thought of as a uniform plateau of lesser extent *subtracted* from the uv -coverage. This introduces a negative bowl around the core of the point spread function (PSF), or dirty beam, which in turn gives rise to negative bowls around regions of positive emission in the dirty map.

2.2. The Ekers-Rots Theorem

Begin by considering the measurement equation, which states the relationship between a single visibility measurement $V(u, v)$ and the sky intensity $I(\ell, m)$:

$$V(u, v) = \iint d\ell dm A(\ell, m) I(\ell, m) e^{-2\pi i(u\ell + vm)} \quad (2)$$

¹The LAS a particular interferometer can accurately recover in a given observations depends on the uv -coverage. There is furthermore not a widely accepted quantitative criterion by which this LAS is judged. Consequently there is some variation in the relationship between LAS and b_{min} that different facilities quote. For example, the ALMA Technical Handbook gives $\theta_{LAS} = 0.6 \lambda/b_{min}$, and the VLA Observational Status Summary gives $\theta_{LAS} = 0.6 \lambda/b_{min}$ to $0.8 \lambda/b_{min}$ for long tracks (half that for snapshots). If this level of discrepancy would substantially impact the science of a proposed project, careful simulations would be in order to determine the suitability of the proposed observations.

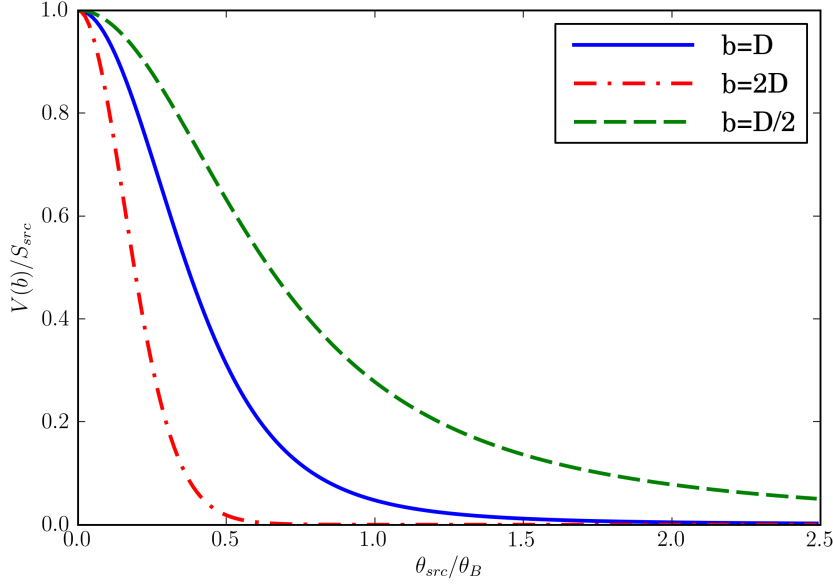


Figure 1. Fraction of total flux density retrieved by an interferometer as a function of the ratio of the (Gaussian) source size to the antenna primary beam, for three different baseline lengths.

Here $A(\ell, m)$ is the antenna primary beam (assumed identical for all antennas); $I(\ell, m)$ is the sky intensity; ℓ and m are sky coordinates; u and v represent the baseline between antennas in wavelengths; and $V(u, v)$ is the measured visibility value. First, note that $V(0, 0)$ is the flux density which would be measured by a single dish telescope with the same primary beam A ; also known as the “zero-spacing” flux². Most of the following also therefore applies to total power measurements with single dish telescopes.

From the convolution theorem, Eq. 2 can be written as

$$V(u, v) = \tilde{A}(u, v) \otimes \tilde{I}(u, v) \quad (3)$$

where $\tilde{I}(u, v)$ is the Fourier transform of the sky intensity and $\tilde{A}(u, v)$ is the Fourier transform of the antenna primary beam. From this it is clear that the antenna primary beam has the effect of a point spread function in uv space: a single visibility measurement $V(u, v)$ has information not only from the Fourier component (u, v) of the ideal sky brightness $\tilde{I}(u, v)$, but also from a range of nearby values determined by the Fourier transform of the primary beam.

Using the fact that the antenna primary beam $A(\ell, m)$ is the magnitude squared of the Fourier transform of the aperture illumination function $E(u, v)$ (Napier 1999; Hunter & Napier 2016) it can also be shown that

$$\tilde{A}(u, v) = E(u, v) \otimes E(u, v)$$

²The term “zero-spacing flux” is sometimes loosely used to mean the total flux density of a given object, although if the source is comparable to or bigger than the primary beam $A(\ell, m)$, the total flux density is greater than the value $V(0, 0)$ that a single-dish having that primary beam would measure.

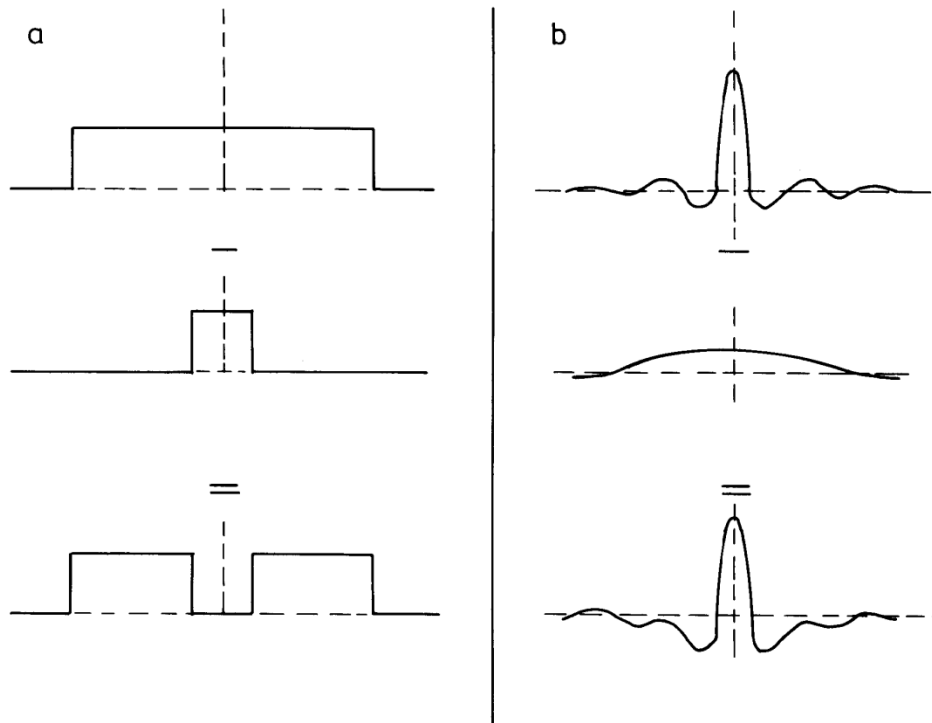


Figure 2. Conceptual illustration of the effect of missing short spacings on an interferometer's synthesized beam. *Left (a):* uv - or aperture-plane coverage; *Right (b):* resulting beam. *Figures from Braun and Walterbos 1985*

i.e., the uv -plane “point-spread function” of an interferometer is the auto-correlation function of the aperture illumination function. For a finite, circular aperture of diameter D , $E(u, v)$ from $(u, v) = 0$ to $\sqrt{u^2 + v^2} = D/2\lambda$. It follows that $\tilde{A}(u, v)$ will typically have support over a region twice as large, *i.e.*, from $(u, v) = (0, 0)$ to $\sqrt{u^2 + v^2} = D/\lambda$. Therefore, a given baseline b contains information not only about the spatial frequency b/λ , but about a whole range of spatial frequencies from $(b - D)/\lambda$ to $(b + D)/\lambda$.

This result is illustrated in Figure 3 : a single visibility measurement on a baseline of (nominal) length b contains information about a range of baseline lengths, from $b - D$ to $b + D$. Similarly, a measurement with a single-dish telescope can be thought of as being a sum of measurements with “baselines” ranging from D to 0. Geometrically it is clear that the single dish measurement has many of the very short spacings and few “baselines” of length $\sim D$; the single dish correspondingly provides greater sensitivity or weight at the shortest spatial frequencies and less at the higher spatial frequencies. Similarly the interferometer provides the highest sensitivity at the spatial frequency b/λ .

The effect of the blurring effect of the primary beam on an interferometer's uv -coverage can be seen in Fig. 4. This is particularly important for the problem of imaging large objects: the “zero-spacing-hole” has shrunk, and the shortest interferometer baseline $b \sim D$ is seen to contain information almost all the way down to $(u, v) = 0$. The very inner-most (lowest spatial frequency) points will have poor signal-to-noise

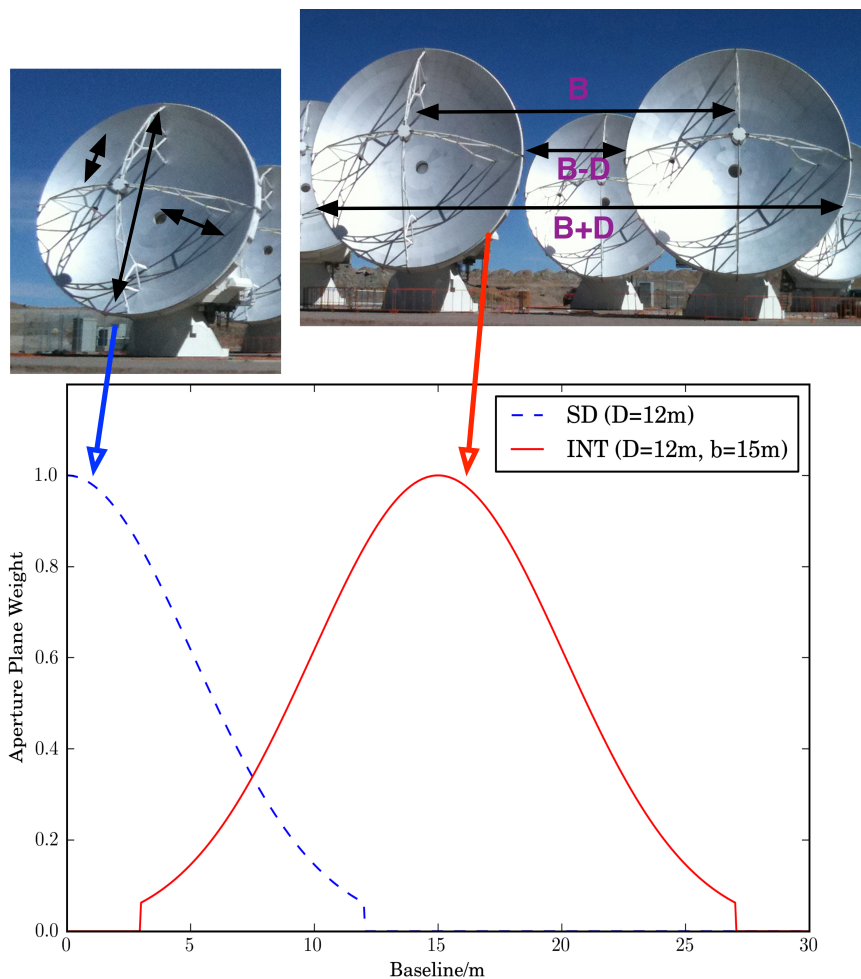


Figure 3. Geometrical interpretation of the range of baselines measured by a single dish (blue, *left*) and a single baseline interferometer (red, *right*).

due to their low weight; these correspond to spatial frequencies of $\sim (3\text{m})/\lambda$ in Fig. 3. The other effect of the primary beam convolution has been to fill in most of the unsampled holes in the aperture plane, at least for this (quite compact) array configuration. If this information can be used it has the potential to stabilize nonlinear deconvolution algorithms like CLEAN (Cornwell et al. 1999).

The problem is that with only a single measurement $V(u, v)$, it is impossible to separately estimate the contributions of the individual Fourier components of the sky brightness. Ekers & Rots (1979) first showed how this limitation can be overcome for an interferometer. By continuously scanning the antennas' pointing positions, making many measurements at different pointing centers on the sky (ℓ', m'), one can tabulate (sample) the function $V(u, v, \ell', m')$. Fourier transforming this function with respect to ℓ' and m' yields an estimate of the sky Fourier transform which has a Fourier resolution determined by the *size of the area scanned over*. If this area is larger than the primary beam, this is a higher Fourier resolution estimate of the sky brightness. It will also allow

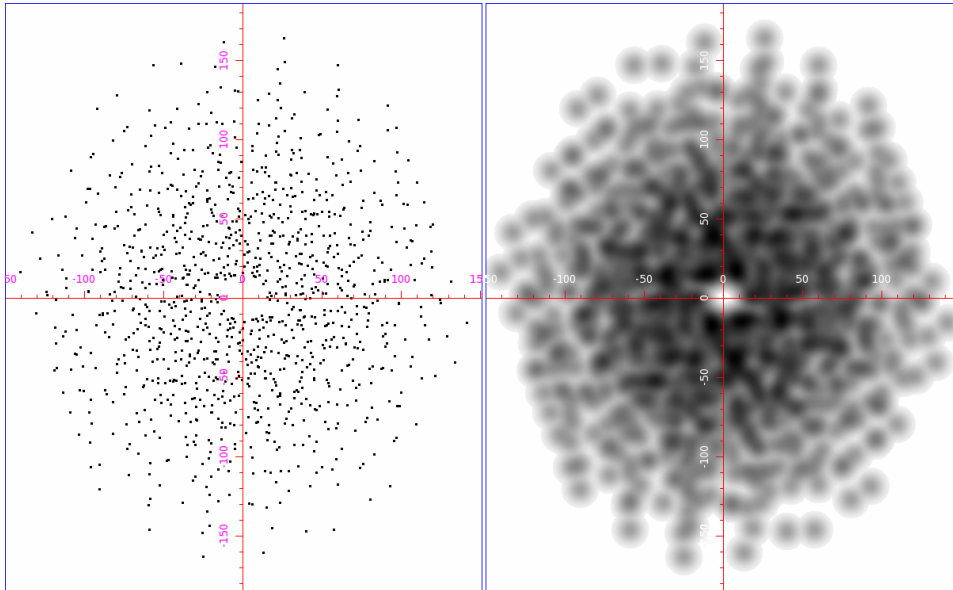


Figure 4. Nominal aperture plane coverage of a single snapshot of a compact ALMA configuration (*left*). The effective aperture plane coverage is shown on the *right*, which is simply the convolution of the points in the left panel with antenna (aperture-plane) primary beam. Note that the units of aperture plane coordinates are *distance* units (in this case, meters). This is a convenient representation of an interferometer’s spatial frequency response when, as is often the case by design, the antenna illumination pattern is approximately wavelength-independent.

estimation of sky components with spatial frequencies all the way down to $(b_{\min} - D)/\lambda$, *i.e.*, less than the spatial frequency given by the shortest physical baseline b_{\min}/λ . A completely analogous argument applies to measurements made by scanning a single dish telescope.

The scheme described by Ekers & Rots gives powerful conceptual insight but suffers from several shortcomings as a practical solution to the short spacing problem. A variety of practical implementations are described in § 3. Among the shortcomings of Ekers-Rots is the fact that what is usually of interest is not a higher resolution estimate of the sky’s Fourier transform, but rather, an improved image of the sky—and in particular, an image which has not been convolved with the interferometer’s synthesized beam. Consequently most practical algorithms which make use of the Ekers-Rots information do so within the context of a deconvolution operation. Additionally, most interferometers do not retain fixed baselines (u, v) with time; rather, the baselines (projected on the sky) change as time progresses. Finally, continuously-scanned interferometric observing has not been commonly available on major radio interferometers until relatively recently.

2.3. Mosaic Observing Strategy & Fourier Space Sampling

Although the argument of Ekers & Rots assumes the interferometer is continuously scanned across the sky, it turns out that continuous scanning is not in fact required. Cornwell (1988) showed that the full Ekers-Rots information can be obtained provided

only that the sky is Nyquist sampled with respect to the antenna primary beam. Cornwell also presented one of the first practical implementations of a deconvolution algorithm which has the benefit of the short-spacing, Ekers-Rots information. This algorithm will be discussed in § 3.2.1.

The Nyquist sampling requirement can be understood as follows. Imagine a single-baseline interferometer with a fixed baseline (u, v) , constructing a rectangular mosaic of pointings spaced by Δ in each of two orthogonal directions on the sky. This will give rise to a series of aliases spaced by $1/\Delta$ in the aperture plane. Each measurement, and each alias, is in fact a measurement over a circular patch³ of uv -space of diameter $2D/\lambda$. Therefore spacing the interferometer pointings $\Delta \leq \lambda/2D \sim \theta_B/2.3$ suffices to prevent the aliases from overlapping the “real” data.

Because the Nyquist-Shannon theorem strictly applies only in one dimension, it is in fact possible to do slightly better than this. A generalization of the Nyquist-Shannon theorem (Petersen & Middleton 1962) can be used to show that in two dimensions the optimal sampling strategy for circularly band-limited functions is a *hexagonally closed packed* lattice. This gives the maximally close-packed arrangement of aliases in Fourier space, and therefore a somewhat more sparse set of telescope pointings in real space. For the case of mosaicking with antennas of diameter D it corresponds to interferometer pointing arranged in equilateral triangles with centers spaced by $\lambda/\sqrt{3}D \sim \theta_B/2$. A hexagonal pattern will require 15% fewer pointings than a rectangular mosaic covering the same region.

For imaging extended emission with an interferometer the recommended practice is to use a hexagonal mosaic with pointing centers spaced by $\lambda/\sqrt{3}D \sim \theta_B/2$ or even closer. If the measurement bandwidth is significant then the shortest wavelength of interest λ_{min} should be used to establish the sampling requirement. In practice, the amount of aliasing caused by slightly undersampling the sky is greatly reduced by the effects of the aperture illumination taper. Therefore for surveying relatively compact sources over large regions considerably more sparse samplings— $0.7\theta_B$ or even $0.8\theta_B$ — are often used to good effect. Note that the anti-aliasing sampling requirements $\lambda/2D$ (for a square mosaic) and $\lambda/\sqrt{3}D$ (for a hexagonal mosaic) are exact and do not require use of an approximate Gaussian beam width. As pointed out by Cornwell (1988), all of these sampling arguments also apply to single-dish mapping.

An approach which has gained wider use recently due to advances in computing and storage speed is *on-the-fly* (or OTF) mosaicking (e.g. Murphy et al. 2010; Lacy et al. 2020). The OTF observing technique is widespread in the single-dish community; Mangum et al. (2007) present an excellent review of the details involved in using OTF in a single dish context. In interferometric OTF mosaicking— just as for single-dish OTF— the antenna pointing positions are continuously and synchronously scanned over the region of astronomical interest on the sky while the visibility data are recorded, usually at a considerably higher data rate than would be necessary for a conventional mosaic. This is also, of course, the observing scheme considered by Ekers & Rots (1979). OTF mosaicking will often provide higher observing efficiency (*i.e.*, lower observing overheads), and can be advantageous in situations where the goal is to map large areas quickly.

³Assuming that the antennas are circular, as is commonly but not always the case.

3. Interferometric Mosaicking Algorithms

In the following sub-sections, I describe the algorithms most commonly used to make images from mosaicked interferometer data.

3.1. Linear Combination of Separately Deconvolved Images

The most straightforward approach to making an image from mosaicked interferometer data is the so-called *linear mosaic*. In a linear mosaic the individual interferometer pointings are deconvolved separately and the resulting deconvolved maps are appropriately weighted and added together to make a final mosaic image. Explicitly, the linear mosaic image I_{LM} formed out of the individual-pointing deconvolved images I_p is:

$$I_{LM}(\mathbf{x}) = \frac{\sum_p A(\mathbf{x} - \mathbf{x}_p) I_p(\mathbf{x}) / \sigma_p^2}{\sum_p A^2(\mathbf{x} - \mathbf{x}_p) / \sigma_p^2} \quad (4)$$

Here σ_p is an estimated or measured noise level for pointing p which is needed to weight the data for optimal sensitivity in beam-overlap regions. For the single-field case this reduces to

$$I_{LM}(\mathbf{x}) = \frac{I_p(\mathbf{x})}{A(\mathbf{x} - \mathbf{x}_p)}$$

which is simply the deconvolved image corrected for the primary beam attenuation.

Linear mosaicking is not usually recommended for imaging extended objects. It suffers from two significant disadvantages for this application, both related to the critical deconvolution step. First, because the visibility data from the individual pointings are never used together, the deconvolution algorithm does not have access to the Ekers-Rots information. Therefore the Fourier resolution and short-spacing information in the deconvolved image will be no better than for a single field. Second, the signal to noise ratio and uv coverage in the individual (dirty) maps used by the deconvolution is worse than in the joint map, particularly in regions of significant overlap between adjacent pointings. This also limits the effectiveness of the deconvolution algorithm, *e.g.*, how deeply it is feasible to clean in order to accurately deconvolve diffuse structures. These problems are exacerbated due to the fact that the deconvolutions used for interferometric imaging are necessarily nonlinear operations.

On the other hand linear mosaicking does offer the possibility of carefully fine-tuning the calibration and deconvolution parameters for each individual pointing. This can be useful when there are significant time and sky position variable effects (such as the ionosphere), or when the field is crowded or confused. For these reasons linear mosaicking is often used at low frequencies (< 1 GHz).

Because it is simply a linear combination of all of the visibilities, a linear mosaic of individual-pointing *dirty images* does in fact contain the full Ekers-Rots information. Since it is convolved with the interferometer synthesized beam—which moreover will vary from pointing to pointing, and thus over the mosaicked dirty image—the joint dirty image mosaic is not useful for most applications. This observation does, however, motivate one of the methods of *joint deconvolution* presented in the next section.

Linear mosaicking is available via the CASA toolkit image toolkit method `linearmosaic`; there is also a prototype implementation in `tclean` accessed by setting `gridder = 'imagemosaic'`. It is available in AIPS through the FLATN task.

3.2. Joint Deconvolution

In order for the deconvolved interferometer image to possess accurate information at spatial frequencies shorter than that of the shortest baseline, it is necessary for the deconvolution algorithm to make use of the visibilities from all of the interferometer pointings (see, *e.g.*, Cornwell 1988; Cornwell et al. 1993; Sault et al. 1996). I will describe three approaches that have been widely used: one that combines the visibility data during deconvolution (§ 3.2.1), and two that combine the visibility data from different pointings before the deconvolution (§ 3.2.2 and § 3.2.3). Note that I use the term “deconvolution” in a broader sense—common in the synthesis imaging community—of estimating the true sky brightness from the incompletely sampled data, rather than the stricter mathematical sense of removing the effects of a spatially invariant point spread function.

3.2.1. “Nonlinear” Joint Deconvolution & Maximum Entropy

CLEAN is a procedure or recipe which decades of use by the community has shown to be quite effective for deconvolution of interferometric data. Its nature as a procedure, however, can make its results and limitations difficult to understand. An alternative approach is to determine the true sky brightness as the solution to a more mathematically simple and well-defined problem. One could, for instance, regard the true (deconvolved) sky as represented by a set of pixel values I_j , all of which are parameters which are varied in a χ^2 fit to the measured visibility data V :

$$\chi^2 = \sum_p \sum_i \frac{|V_{p,i} - V_{p,i}^M|^2}{\sigma_{p,i}^2} \quad (5)$$

Here the model visibility values $V_{p,i}^M$ for each pointing p are obtained by Fourier transforming the sky model I_j using the measurement equation. Due to the finite sampling of uv space, this minimization is not generally a well-posed or stable problem: this is the “ghost distributions” problem discussed in Cornwell et al. (1999).

Cornwell (1988) introduced a practical algorithm for deconvolving mosaicked interferometer data which, instead, aims to maximize the so-called *Entropy*

$$H = - \sum_j I_j \ln \left(\frac{I_j}{M_j e} \right) \quad (6)$$

subject to the constraint that χ^2 —Eq. 5—is close to its expected value. In Eq. 6, M_j is a “default image” which is an input to the deconvolution process. In the absence of other information it is typically taken to be a constant. The H term serves to regularize the otherwise ill-posed inversion problem and thereby select one of the infinitely many surface brightness distributions which are consistent with the measured visibilities. Cornwell (1988) called this method “Nonlinear Mosaicking”. It is commonly referred to in the synthesis imaging literature as the Maximum Entropy Method (MEM). A general review of the MEM technique is given by Narayan & Nityananda (1986).

Maximizing the entropy term has the effect of compressing the range of pixel values (relative to the default image) in the solution. This tends therefore to produce smoother images than CLEAN, and is naturally suited to imaging extended emission.

The images MEM produces are biased for two reasons: the pixel values I_j in the solution must be positive; and the effect of the entropy term H is typically to move the solution away from solutions which strictly minimize χ^2 alone. Means of minimizing this bias will be discussed more in § 3.3. One attractive property of MEM is that it provides a straightforward method to provide single dish information to the joint, interferometric deconvolution: the single dish data can be used as the default image M_j (§ 4).

A version of the MEM mosaic deconvolver is implemented in AIPS as the tasks UTESS and VTESS, and is available in the CASA toolkit.

3.2.2. Deconvolution of Combined Dirty Maps

Another approach to imaging mosaicked interferometer data takes as its starting point the linear mosaic of dirty maps from all pointings:

$$I_{joint}^D(\mathbf{x}) = W(\mathbf{x}) \frac{\sum_p A(\mathbf{x} - \mathbf{x}_p) I_p^D(\mathbf{x}) / \sigma_p^2}{\sum_p A^2(\mathbf{x} - \mathbf{x}_p) / \sigma_p^2} \quad (7)$$

$W(\mathbf{x})$ here is an apodization function used to suppress noise artifacts at the edge of the mosaic. As previously noted this joint dirty map contains all of the information that the visibilities together do, but not in a very convenient form since it is convolved with a messy point spread function. In fact for an image formed according to Eq. 7, the PSF will typically be spatially variable since the uv coverage and noise generally change from one interferometer pointing to the next. This approach is often referred to simply as “joint deconvolution”.

Given a method of calculating the PSF this I_{joint}^D can be deconvolved by the usual means, *e.g.* CLEAN or MEM. Cornwell et al. (1993) studied a method employing an approximate PSF evaluated at the center of the mosaic; CASA’s `tclean` task, invoked with `gridder='standard'`, uses a variant of this algorithm. Sault et al. (1996) present an exact expression for the position-dependent PSF of the map in Eq. 7; they also present an image projection designed to minimize w-term distortions. MIRIAD implements this form of joint deconvolution using in tasks `MOSSDI` (which uses CLEAN for the deconvolution) and `MOSMEM` (which uses MEM instead). Use of MEM for the deconvolution of the joint dirty map (Eq. 7) is very similar to the strategy outlined in § 3.2.1, but with the χ^2 of the sky model with respect to the data evaluated in the image rather than visibility domain.

This approach to joint deconvolution has been widely used and is a good option for imaging significantly extended objects with an interferometer.

3.2.3. Wide-field Imaging

A more modern approach to imaging mosaicked interferometer data is to reference all pointings’ data to a single phase center and grid them onto a common uv -plane. This results in a single PSF with improved uv -coverage for the whole mosaic and an optimal-sensitivity weighting of the data. This approach is described in detail in (Myers et al. 2003) but a brief outline is as follows. First, we can write the measurement equation for a given visibility $\mathbf{u}_k = (u_k, v_k)$, for a mosaic pointing at $\mathbf{x}_p = (\ell_p, m_p)$, and with an explicit phase tracking center $\mathbf{x}_{\phi,p}$, as:

$$V_p(\mathbf{u}_k) = \int \int \mathbf{d}^2\mathbf{x} A(\mathbf{x} - \mathbf{x}_p) I(\mathbf{x}) e^{-2\pi i \mathbf{u}_k \cdot (\mathbf{x} - \mathbf{x}_{\phi,p})} \quad (8)$$

Using the shift theorem this can be re-expressed as an integral in the aperture plane as

$$V_p(\mathbf{u}_k) = e^{2\pi i(\mathbf{u}_k \cdot \mathbf{x}_{\phi,p})} \int \int d^2\mathbf{u} \tilde{A}(\mathbf{u}_k - \mathbf{u}) \tilde{I}(\mathbf{u}) e^{2\pi i(\mathbf{u} - \mathbf{u}_k) \cdot \mathbf{x}_p}. \quad (9)$$

This relationship can, in essence, be inverted to obtain a set of estimators $\tilde{I}_j = \tilde{I}(\mathbf{u}_j)$ of the Fourier transform of the sky brightness on a grid of points \mathbf{u}_j . The cell size of the grid \mathbf{u}_j is determined by the angular extent of the mosaic on the sky and the estimators themselves are simply linear combinations of the original visibility data with appropriate phase gradients and normalizations. To the extent that the aperture plane illumination $\tilde{A}(\mathbf{u}_k - \mathbf{u})$ is correct, the “blurring” effect of the interferometer primary beam will have been removed from the \tilde{I}_j , which will have a resolution determined by the mosaic size. These visibility estimators can be imaged by standard techniques such as CLEAN.

This approach makes optimal use of the whole range of aperture plane information inherent in the data and provides a natural basis on which to incorporate wide-field effects such as W-projection and A-projection. It is also well-suited to jointly imaging data from a heterogeneous interferometer, *i.e.*, one in which the antenna sizes are not identical. One drawback to this approach is that it relies upon an accurate model of the antenna primary beam. It can also be computationally expensive, though it is faster when there are many pointing centers in the mosaic, such as there are for an OTF mosaic. It is generally the preferred approach for mosaicking extended structures when using CLEAN in CASA. The `tclean` task uses this algorithm when `gridding='mosaic'` is set in its invocation.

3.3. Practical Challenges in Deconvolution

Even with the benefit of the information provided by the joint mosaic pointings’ visibilities, imaging extended emission with an interferometer can be challenging. It is therefore important to understand the characteristics of the deconvolution algorithm used. Here I summarize some relevant, key properties of the two dominant approaches used by the synthesis imaging community: CLEAN and Maximum Entropy.

Since CLEAN represents the sky as a sum of *unresolved* signals (or “point sources”), it can take many iterations to construct a model of a significantly extended source. In general, it is advisable to clean interactively; to carefully define the regions used for cleaning so as to contain only ostensibly real and believable signal; and to iteratively inspect and refine these regions through the cleaning process (*e.g.*, after each major cycle). For imaging extended emission, the CLEAN threshold chosen can have a significant effect on the resulting image. For instance, a 3σ threshold will leave a plateau of un-deconvolved signal of approximately this amplitude (with the corresponding “short spacing bowl” around it). This effect can be mitigated by cleaning deeply, *e.g.*, down to a 1.5σ threshold. Such deep cleaning will result in some spurious noise components in the CLEAN model. This is often acceptable since the science image is usually taken to be the sum of the (CLEAN-beam convolved) model and the residuals, and to first order the deep cleaning will simply have re-partitioned the noise between the model and the residuals. It is potentially more problematic if the CLEAN model is to be used for self calibration. Such deep cleaning can also be very time-consuming for spectral line cubes with many channels.

There are two other biases worth bearing in mind when using CLEAN to image extended objects. One is the flux bias resulting from the mismatch between the clean

and dirty beam areas, discussed by Jorsater & van Moorsel (1995) and Walter et al. (2008). These authors give an analytic correction for the effect, and note that it is also mitigated by deeper cleaning. Another is the so-called “CLEAN bias” discussed in, *e.g.*, Condon et al. (1998). The CLEAN bias results from the constructive interference of the sidelobes of the synthesized beam. Particularly for diffuse, extended sources, these sidelobes can then be brighter in the dirty map than the apparent signal in the main lobe of the PSF. This biases the recovered flux densities low and is mitigated by careful masking and better uv coverage. All of that said, CLEAN is the algorithm most commonly used for synthesis imaging, and when carefully applied will generally yield excellent results if the data are of sufficient quality.

A variety of techniques have been developed to improve the performance of CLEAN for extended sources. These include Multi-Scale CLEAN (Cornwell 2008) and ASP-clean (Bhatnagar & Cornwell 2004), and involve using CLEAN components of varying sizes. These algorithms can improve the stability and convergence speed when imaging extended objects. Multi-scale CLEAN is available within CASA’s `tclean` task by setting `deconvolver = multiscale`.

Maximum Entropy Deconvolution (MEM) is naturally well-suited to image extended emission. By definition it is a biased estimator of the true sky image since the effect of including of an entropy term is to move the solution away from the minimum of χ^2 (§ 3.2.1). For $\text{SNR} \gg 1$ this bias is negligible. The bias is also reduced by using an appropriate default image, *e.g.*, a single-dish image. The resolution of MEM-reconstructed images is also known to vary with SNR; the impact of this can be reduced by convolving the MEM image with a nominal synthesized beam, much as is done with a CLEAN model. Finally, MEM has great difficulty with point sources embedded in diffuse emission. In this circumstance it is best to remove the point source by other means (such as CLEAN) prior to MEM deconvolution.

Finally, different implementations of these deconvolution algorithms often contain subtle (or not subtle) differences, and the performance of algorithms can vary between implementations. If the application is demanding— and imaging diffuse emission often is— it can be helpful to consult or collaborate with an expert.

4. Combining Interferometric and Single-Dish Data

Often when the source of interest is comparable in size to the interferometer primary beam the best course of action is to obtain single-dish data and to combine the two datasets. A variety of techniques has been developed to do this. An excellent review and comparison of techniques used to combine interferometric and single dish data is given by Stanimirovic (2002). Here— because it is straightforward, widely used, and robust— I will focus mainly on a technique to linearly combine the single dish and interferometer data in uv space known as “feathering”. Cotton (2017) discusses the technique in detail.

To understand feathering, it is useful first to consider the nature of the low spatial frequency components in an interferometer map which has been deconvolved using CLEAN. Although the interferometer does not accurately measure these spatially large signals there is not usually an explicit constraint on the total flux density in the CLEAN model: for instance, it is not generally zero. Therefore CLEAN will *extrapolate* the values of spatial frequencies smaller than the smallest measured. Often this extrapo-

lation will be very noisy. It is desirable to down-weight this low-quality information where better quality (single dish) information is available.

To feather single dish and interferometric maps together, the individual datasets are first deconvolved separately to remove the effects of their respective point spread function. Each deconvolved map is then Fourier transformed and the interferometer map is high-pass filtered— with a characteristic scale determined by the diameter D_{SD} of the single dish telescope— to eliminate the poorly determined large-scale information in it. The maps are then added together and inverse Fourier transformed to obtain a single image with information from both datasets. In more detail, the sequence of steps typically required is as follows:

1. Prepare input images.
 - (a) Deconvolve the synthesized beam from the interferometric dirty map, *e.g.* using CLEAN. The resulting model is usually then re-convolved with a nominal “restoring” beam (of FWHM $\theta_{B,int}$) to obtain the deconvolved interferometric map I_{int} in units of Janskys per (restoring) beam. This nominal beam is almost always taken to be a Gaussian.
 - (b) Deconvolve the antenna beam from the single dish map and re-convolve it with a nominal restoring beam ($\theta_{B,SD}$) to obtain the deconvolved single dish map I_{SD} in Janskys per (restoring) beam. Since the single dish data in principle sample all spatial frequencies out to the maximum (D_{SD}/λ), simple linear methods can sometimes be used instead of the non-linear methods required by the interferometric imaging problem. If the single-dish beam is simple enough to be well-approximated by a Gaussian, this step can be omitted. If there is considerable overlap between the interferometer and the single dish in uv -space, it may be desirable to use a restoring beam larger than the antenna primary beam to give relatively greater weight to the interferometer data at the higher spatial frequencies.
 - (c) Various implementation-dependent clerical steps may also be required. For example: ensuring the map sizes, registrations, and pixellizations are appropriate; correcting for the primary beams; re-ordering axes; padding and apodizing maps as needed to avoid edge effects; and putting restoring beam information in image headers.
2. Place the deconvolved maps on a common surface brightness scale. This can be done, for example, by multiplying I_{SD} by $(\theta_{B,int}/\theta_{B,SD})^2$, or by converting both maps into instrument-independent surface brightness units such as Janskys per Steradian.
3. Fourier transform the maps to obtain $\tilde{I}_{SD}(u, v)$ and $\tilde{I}_{int}(u, v)$.
 - (a) It is often useful at this stage to correct any (hopefully slight) errors in the relative calibration of the single-dish and interferometric maps, *e.g.*, due to the flux scale assumed. This can be done by deriving a scale factor f_{cal} from comparing the Fourier transforms of I_{SD} and I_{int} in the range of uv values well-measured by each, properly accounting for the restoring beam of each.
 - (b) “feather” the images together in the Fourier domain using a taper function $T(u, v) = 1 - \tilde{B}_{SD}$ as

$$\tilde{I}_{combined}(u, v) = \tilde{I}_{SD}(u, v) + \tilde{I}_{int}(u, v) \times (1 - \tilde{B}_{SD}) \quad (10)$$

where \tilde{B}_{SD} is the Fourier transform of the single dish restoring beam normalized to have a peak of one. An example interferometer re-weighting function suitable for combining GBT and VLA C-configuration data is shown in Figure 5. The taper function has the effect of emphasizing each dataset where it provides the best information while minimizing excessive noise that will be introduced by over-weighting data in poorly measured regions of the uv plane.

4. Inverse Fourier transform to obtain the image $I_{combined}$, containing information from both the single dish and the interferometer.

This algorithm is implemented in CASA as `feather`⁴, in AIPS as `IMERG`, and in MIRIAD as `IMMERGE`. These implementations differ in the details of how the restoring beams and feathering weights are defined and handled, but typically take the deconvolved interferometer and single dish maps and their beams θ_{SD} , θ_{int} as input and perform steps 2 - 4 of the above. They also assume that the restoring beams are Gaussian. In particular, as described in step 1(b) above, if the single-dish beam significantly deviates from a Gaussian shape—*e.g.* due to sidelobes or ellipticity—then its effects should be removed from the map by deconvolution (see, *e.g.*, Weiß et al. 2001). Two of many examples of the application of the feathering technique in the literature are Vogel et al. (1984) and Dubner et al. (1998).

For feathering to work well there should be region of the uv plane measured by both the interferometer and the single dish. A commonly adopted criterion is for the diameter of the single dish D_{SD} to be 1.5 to 2 times larger than the minimum baseline b_{min} in the interferometric array. By this criterion, for instance, the 100-meter GBT is well-suited to provide short-spacing data for EVLA C- or D-configuration data. This criterion also implies that an interferometric array with antennas of a single diameter cannot even in principle provide high-quality total power data for itself by measuring auto-correlations or outfitting some of the antennas with total power receivers.

Another approach to combining single dish and interferometric data is to do so before or during the deconvolution. This has the advantage of providing considerably more information to the nonlinear interferometric deconvolution. One method, mentioned previously in § 3.2.1, is to use the single-dish data as the “default image” in a Maximum Entropy deconvolution of the interferometric image. Another method is to directly form a linear combination of the single-dish and interferometer “dirty” images, pre-deconvolution. In this case the effective beam is the corresponding linear combination of the respective single-dish and interferometer point spread functions; the image can then be deconvolved by the usual methods. These techniques are discussed and compared in greater detail in Stanimirovic (2002), beautifully applied to 21-cm mosaic maps of the Small Molecular Cloud from Parkes and the ACTA. Two recently developed, alternative approaches which fold single dish data into the deconvolution process are the so-called TP2VIS (Koda et al. 2011, 2019) and SDINT (Rau et al. 2019) methods. One attractive feature of these methods is that they naturally accommodate deconvolution of the single-dish PSF (primary beam).

⁴A word of caution: the `sdfactor` keyword of CASA’s `feather` task is not a weight, it is a direct scaling factor applied to the single dish data. As such, values other than the default (1.0) should be set with caution, and a clear and quantitative physical motivation.

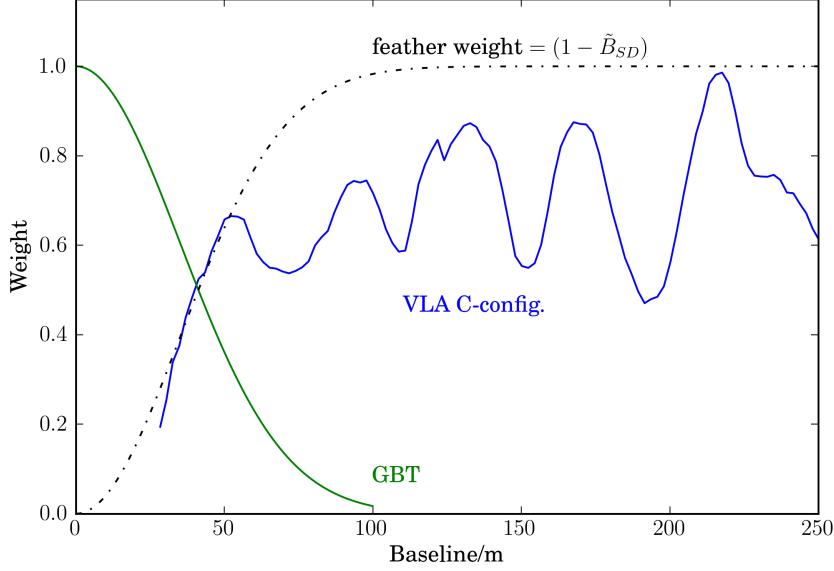


Figure 5. Relative aperture-plane sensitivities of GBT and the C-configuration of the VLA and an appropriate feathering weight which could be used to combine the two.

The relative weights of the single dish and interferometer data will strongly affect the characteristics of the combined image. These can be set or adjusted manually but the best quality images are obtained when the relative weights are determined by the intrinsic noise properties of each dataset. Therefore it is important that the sensitivities of the single dish and interferometric maps or cubes are well matched. Two useful criteria are to match the single dish and interferometer sensitivities in overlapping regions of the aperture plane (Kurono et al. 2009; Koda et al. 2011; Mason & Brogan 2014) and to obtain single dish data which result in an overall distribution of uv -plane weights which is smooth and approximately Gaussian (Rodríguez-Fernández et al. 2008). When combining with data from modern interferometer arrays, the implied requirement on the single dish map sensitivity is sufficiently stringent that large aperture single dishes and/or focal plane arrays are often advantageous.

An illustration of the improvement that can be made by adding single-dish data to an interferometer map is shown in Figure 6. This is a simulated observation⁵ of a nearby galaxy, $\sim 1'$ in size, using ALMA at $\lambda = 0.9$ mm. ALMA consists of 50 12-m antennas operating as an interferometer, with an additional 4 12-m antennas operated as single dishes to provide total power; 12 7-m antennas operated as an interferometer to bridge the gap in the aperture plane between them. In this simulated observation, the ALMA 12-m primary beam is $19''$ (FWHM); 67 pointings of the 12-m ALMA array on a hexagonal lattice are used to cover the field of interest, and 23 pointings of

⁵This simulation and imaging exercise uses sample data and scripts available on <http://casaguides.nrao.edu/>.

the 7-m array. These 12-m and 7-m interferometric data were deconvolved using the wide-field CLEAN algorithm implemented in CASA (§ 3.2.3). The resulting CLEAN image is shown in the left panel. In spite of the considerable improvement in sensitivity to large spatial scales that the 7-m array provides, substantial negative bowls are still evident around the source. The right panel shows the image resulting from combining the interferometric and total power maps using feather.

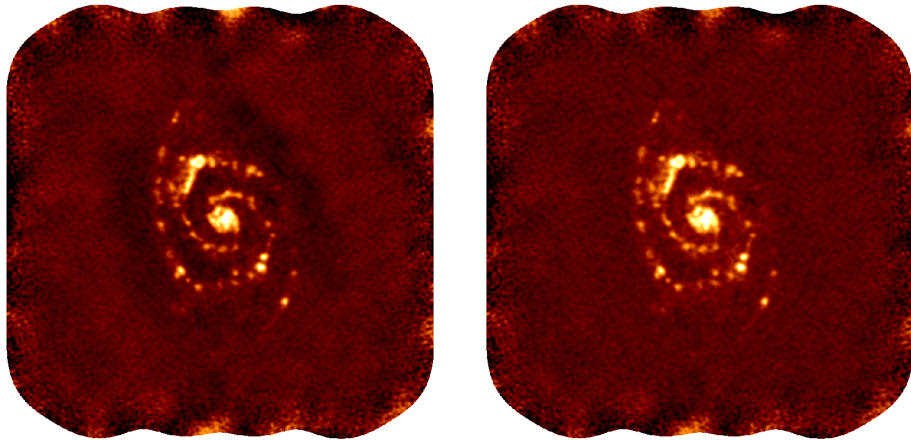


Figure 6. *Left*: Simulated ALMA 12m+7m $\lambda = 0.9$ mm interferometric mosaic of a galaxy 1' in size (ALMA 12-m primary beam: 19'' FWHM). *Right*: after adding 12m total power data using the feather algorithm.

5. Practical Issues

Following is a brief summary of some of the practical effects that need to be considered when planning and analyzing mosaicked interferometric observations and single dish observations intended to support them.

- Choose an appropriate mosaic sampling strategy (§ 2.3). For high-fidelity imaging of extended emission, a hexagonal mosaic with pointing centers spaced by $\lambda/\sqrt{3}D$ is preferable. Faster sky coverage can be achieved with sparser coverage, although this will not perform as well for retrieving short spacings, and will require more accurate knowledge of the primary beam.
- Many effects can cause the interferometer imaging characteristics to vary from one mosaic pointing to another. This will tend to degrade the resulting image quality, depending on the reconstruction approach adopted. For instance, the uv coverage will change due to the Earth's rotation; flagging; the system temperature— hence noise— can vary; at short wavelengths the tropospheric

phase can vary; and at long wavelengths ionospheric effects will vary. Multiple coverages of the mosaic will tend to average such variations out, improving image quality, at the price of lower observing efficiency.

- Minimizing antenna pointing errors is more important for interferometric mosaics than for single pointings. In the single-pointing case, the strongest emission is typically in the center of the beam, which is relatively flat; in the case of a mosaic, there is generally emission over the entire field, including areas where the primary beam has a steep gradient.
- If single dish data is required, it is desirable that the dish diameter be at least $1.5\times$ the minimum baseline in the interferometer, and preferably more. This is required to provide adequate uv coverage and to be able to accurately link the calibration of the two instruments.
- Single dish pointing errors can introduce spurious high spatial frequency structure to the map. These can often be alleviated by lightly smoothing.
- The single dish antenna may have a non-trivial beam (*e.g.*, due to an error beam, shadowing of the primary, *etc.*) requiring deconvolution.
- Depending on the calibration and imaging algorithms used the single dish map may have accurate information over only a limited range of spatial frequencies, not all the way down to $(u, v) = 0$. This is particularly true for continuum data, which by definition lack a spectral dimension to help distinguish systematic effects from astronomical signal.
- Ensure that the single dish map is sufficiently sensitive to provide useful information, and has a guard band of at least a few single-dish beams around the source.

Acknowledgments. The National Radio Astronomy Observatory is a facility of the National Science Foundation operated by Associated Universities, Inc. This text is based on lectures given by the author at the 14th, 15th, and 16th NRAO Synthesis Imaging Summer Schools, and I thank the organizing committees for doing the hard work of getting together and running these workshops. I am also grateful to those who covered this topic at previous summer schools, especially Jurgen Ott and Steve Myers. I thank Urvashi Rau and Crystal Brogan for helpful discussions, and Jeff Mangum and Adele Plunkett for comments on this manuscript.

References

- Bhatnagar, S., & Cornwell, T. J. 2004, A&A, 426, 747. [astro-ph/0407225](#)
- Condon, J. J., Cotton, W. D., Greisen, E. W., Yin, Q. F., Perley, R. A., Taylor, G. B., & Broderick, J. J. 1998, AJ, 115, 1693
- Cornwell, T., Braun, R., & Briggs, D. S. 1999, in Synthesis Imaging in Radio Astronomy II, edited by G. B. Taylor, C. L. Carilli, & R. A. Perley, vol. 180 of Astronomical Society of the Pacific Conference Series, 151
- Cornwell, T. J. 1988, A&A, 202, 316
- 2008, IEEE Journal of Selected Topics in Signal Processing, 2, 793
- Cornwell, T. J., Holdaway, M. A., & Uson, J. M. 1993, A&A, 271, 697
- Cotton, W. D. 2017, PASP, 129, 094501. [1707.02272](#)
- Dubner, G. M., Holdaway, M., Goss, W. M., & Mirabel, I. F. 1998, AJ, 116, 1842

- Ekers, R. D., & Rots, A. H. 1979, in IAU Colloq. 49: Image Formation from Coherence Functions in Astronomy, edited by C. van Schooneveld, vol. 76 of Astrophysics and Space Science Library, 61
- Hunter, T. R., & Napier, P. J. 2016, arXiv e-prints, arXiv:1609.09376. 1609.09376
- Jorsater, S., & van Moorsel, G. A. 1995, AJ, 110, 2037
- Koda, J., Sawada, T., Wright, M. C. H., Teuben, P., Corder, S. A., Patience, J., Scoville, N., Donovan Meyer, J., & Egusa, F. 2011, ApJS, 193, 19
- Koda, J., Teuben, P., Sawada, T., Plunkett, A., & Fomalont, E. 2019, PASP, 131, 054505. 1903.07611
- Kurono, Y., Morita, K.-I., & Kamazaki, T. 2009, PASJ, 61, 873
- Lacy, M., Baum, S. A., Chandler, C. J., Chatterjee, S., Clarke, T. E., Deustua, S., English, J., Farnes, J., Gaensler, B. M., Gugliucci, N., Hallinan, G., Kent, B. R., Kimball, A., Law, C. J., Lazio, T. J. W., Marvil, J., Mao, S. A., Medlin, D., Mooley, K., Murphy, E. J., Myers, S., Osten, R., Richards, G. T., Rosolowsky, E., Rudnick, L., Schinzel, F., Sivakoff, G. R., Sjouwerman, L. O., Taylor, R., White, R. L., Wrobel, J., Andernach, H., Beasley, A. J., Berger, E., Bhatnager, S., Birkinshaw, M., Bower, G. C., Brandt, W. N., Brown, S., Burke-Spolaor, S., Butler, B. J., Comerford, J., Demorest, P. B., Fu, H., Giacintucci, S., Golap, K., Güth, T., Hales, C. A., Hiriart, R., Hodge, J., Horeh, A., Ivezić, Ž., Jarvis, M. J., Kamble, A., Kassim, N., Liu, X., Loinard, L., Lyons, D. K., Masters, J., Mezcu, M., Moellenbrock, G. A., Mroczkowski, T., Nyland, K., O'Dea, C. P., O'Sullivan, S. P., Peters, W. M., Radford, K., Rao, U., Robnett, J., Salcido, J., Shen, Y., Sobotka, A., Witz, S., Vaccari, M., van Weeren, R. J., Vargas, A., Williams, P. K. G., & Yoon, I. 2020, PASP, 132, 035001. 1907.01981
- Mangum, J. G., Emerson, D. T., & Greisen, E. W. 2007, A&A, 474, 679. 0709.0553
- Marvil, J. 2018, Online Proceedings of the 16th NRAO Synthesis Imaging Workshop. Accessed: 2020-06-02, URL <https://science.nrao.edu/science/meetings/2018/16th-synthesis-imaging-workshop/16th-synthesis-imaging-workshop-lectures>
- Mason, B., & Brogan, C. 2014, ALMA Memo 598
- Mioduszewski, A. 2014, Online Proceedings of the 14th NRAO Synthesis Imaging Workshop. Accessed: 2020-06-02, URL <https://science.nrao.edu/science/meetings/2014/14th-synthesis-imaging-workshop/lectures>
- Murphy, T., Sadler, E. M., Ekers, R. D., Massardi, M., Hancock, P. J., Mahony, E., Ricci, R., Burke-Spolaor, S., Calabretta, M., Chhetri, R., de Zotti, G., Edwards, P. G., Ekers, J. A., Jackson, C. A., Kesteven, M. J., Lindley, E., Newton-McGee, K., Phillips, C., Roberts, P., Sault, R. J., Staveley-Smith, L., Subrahmanyan, R., Walker, M. A., & Wilson, W. E. 2010, MNRAS, 402, 2403. 0911.0002
- Myers, S. T., Contaldi, C. R., Bond, J. R., Pen, U.-L., Pogossyan, D., Prunet, S., Sievers, J. L., Mason, B. S., Pearson, T. J., Readhead, A. C. S., & Shepherd, M. C. 2003, ApJ, 591, 575. astro-ph/0205385
- Napier, P. 1999, in Synthesis Imaging in Radio Astronomy II, edited by G. B. Taylor, C. L. Carilli, & R. A. Perley, vol. 180 of Astronomical Society of the Pacific Conference Series, 37
- Narayan, R., & Nityananda, R. 1986, ARA&A, 24, 127
- Petersen, D. P., & Middleton, D. 1962, Information and Control, 5, 279
- Rau, U., Naik, N., & Braun, T. 2019, AJ, 158, 3. 1904.08867
- Rodríguez-Fernández, N., Pety, J., & Gueth, F. 2008, IRAM technical memo 2008-2
- Sault, R. J., Staveley-Smith, L., & Brouw, W. N. 1996, A&AS, 120, 375
- Stanimirovic, S. 2002, in Single-Dish Radio Astronomy: Techniques and Applications, edited by S. Stanimirovic, D. Altschuler, P. Goldsmith, & C. Salter, vol. 278 of Astronomical Society of the Pacific Conference Series, 375. astro-ph/0205329
- Taylor, G. B., Carilli, C. L., & Perley, R. A. (eds.) 1999, vol. 180 of Astronomical Society of the Pacific Conference Series
- Thompson, A. R., Moran, J. M., & Swenson, J., George W. 2017, Interferometry and Synthesis in Radio Astronomy, 3rd Edition

- Vogel, S. N., Wright, M. C. H., Plambeck, R. L., & Welch, W. J. 1984, ApJ, 283, 655
- Walter, F., Brinks, E., de Blok, W. J. G., Bigiel, F., Kennicutt, R. C., Jr., Thornley, M. D., & Leroy, A. 2008, AJ, 136, 2563. [0810.2125](#)
- Weiß, A., Neininger, N., Hüttemeister, S., & Klein, U. 2001, A&A, 365, 571. [astro-ph/0010541](#)